

Probing nickelate superconductors at atomic scale: A STEM review

Yihan Lei(雷一涵), Yanghe Wang(王扬河), Jiahao Song(宋家豪), Jinxin Ge(葛锦昕), Dirui Wu(伍迪睿), Yingli Zhang(张英利), and Changjian Li(黎长建)

Citation: Chin. Phys. B, 2024, 33 (**9**): 096801. DOI: 10.1088/1674-1056/ad6a0d
Journal homepage: http://cpb.iphy.ac.cn; http://iopscience.iop.org/cpb

What follows is a list of articles you may be interested in

Symmetry quantification and segmentation in STEM imaging through Zernike moments

Jiadong Dan, Cheng Zhang, Xiaoxu Zhao(赵晓续), and N. Duane Loh
Chin. Phys. B, 2024, 33 (**8**): 086803. DOI: 10.1088/1674-1056/ad51f4

Anomalous strain effect in heteroepitaxial $SrRuO_3$ films on (111) $SrTiO_3$ substrates

Zhenzhen Wang(王珍珍), Weiheng Qi(戚炜恒), Jiachang Bi(毕佳畅), Xinyan Li(李欣岩), Yu Chen(陈雨), Fang Yang(杨芳), Yanwei Cao(曹彦伟), Lin Gu(谷林), Qinghua Zhang(张庆华), Huanhua Wang(王焕华), Jiandi Zhang(张坚地), Jiandong Guo(郭建东), and Xiaoran Liu(刘笑然)
Chin. Phys. B, 2022, 31 (**12**): 126801. DOI: 10.1088/1674-1056/ac8725

Fabrication of $GaAs/SiO_2/Si$ and GaAs/Si heterointerfaces by surface-activated chemical bonding at room temperature

Rui Huang(黄瑞), Tian Lan(兰天), Chong Li(李冲), Jing Li(李景), and Zhiyong Wang(王智勇)
Chin. Phys. B, 2021, 30 (**7**): 076802. DOI: 10.1088/1674-1056/abf917

High-resolution electron microscopy for heterogeneous catalysis research

Yong Zhu(朱勇), Mingquan Xu(许名权), Wu Zhou(周武)
Chin. Phys. B, 2018, 27 (**5**): 056804. DOI: 10.1088/1674-1056/27/5/056804

Aberration-corrected scanning transmission electron microscopy for complex transition metal oxides

Qing-Hua Zhang(张庆华), Dong-Dong Xiao(肖东东), Lin Gu(谷林)
Chin. Phys. B, 2016, 25 (**6**): 066803. DOI: 10.1088/1674-1056/25/6/066803

TOPICAL REVIEW — Stephen J. Pennycook: A research life in atomic-resolution STEM and EELS

Probing nickelate superconductors at atomic scale: A STEM review

Yihan Lei(雷一涵)[1,2], Yanghe Wang(王扬河)[1,2], Jiahao Song(宋家豪)[1,2], Jinxin Ge(葛锦昕)[1,2], Dirui Wu(伍迪睿)[1,2], Yingli Zhang(张英利)[1,2], and Changjian Li(黎长建)[1,2,†]

[1] *Department of Materials Science and Engineering, Southern University of Science and Technology, Shenzhen* 518055, *China*

[2] *Guangdong Provincial Key Laboratory of Functional Oxide Materials and Devices, Southern University of Science and Technology, Shenzhen* 518055, *China*

(Received 7 June 2024; revised manuscript received 1 August 2024; accepted manuscript online 1 August 2024)

The discovery of nickelate superconductors, including doped infinite-layer (IL) nickelates RNiO$_2$ (R = La, Pr, Nd), layered square-planar nickelate Nd$_6$Ni$_5$O$_{12}$, and the Ruddlesden–Popper (RP) phase La$_3$Ni$_2$O$_7$, has spurred immense interest in fundamental research and potential applications. Scanning transmission electron microscopy (STEM) has proven crucial for understanding structure–property correlations in these diverse nickelate superconducting systems. In this review, we summarize the key findings from various modes of STEM, elucidating the mechanism of different nickelate superconductors. We also discuss future perspectives on emerging STEM techniques for unraveling the pairing mechanism in the "nickel age" of superconductivity.

Keywords: scanning transmission electron microscopy, superconductivity, epitaxial thin films, nickelates

PACS: 68.37.Ma, 74.25.Dw, 81.30.Dz, 79.20.Uv **DOI:** 10.1088/1674-1056/ad6a0d

1. Introduction

Ni-based superconductors were proposed long ago[1] due to their similarity to Cu-based superconductors. Ni^+ is isoelectronic to Cu^{2+}, with d^9 electronic configuration, but Ni^+ is not the most stable oxidation state. Crespin *et al.* reported the first stable LaNiO$_2$ phase obtained via H$_2$ reduction from LaNiO$_3$ in 1983.[2,3] Later, NdNiO$_{2+x}$ was successfully synthesized using a metal hydride reduction approach in 2003,[4] with the phase transition found to be reversible.[5] The exact structure was clearly resolved using aberration-corrected scanning transmission microscopy (AC-STEM) in 2016.[6] However, the search for nickelate superconductors remained unsuccessful until 2019, when Li *et al.*[7] reported the first conclusive evidence of superconductivity in Nd$_{0.8}$Sr$_{0.2}$NiO$_2$ films, achieving a critical temperature T_c of $\sim$ 9 K–15 K through topotactic reduction with CaH$_2$ at 260 °C–280 °C for 4 hours–6 hours.

This ground-breaking discovery sparked a surge of studies[8–12] aimed at understanding superconductivity and pushing the critical temperature to higher values. Within the infinite-layer (IL) nickelate system, specifically the doped RNiO$_2$ system (R = Nd,[7,12,13] Pr,[8] La[10,11]), the highest IL superconducting temperature is $\sim$ 30 K , achieved in Pr$_{1.82}$Sr$_{0.18}$NiO$_2$ under hydrostatic pressure.[14] Additionally, a more general form of IL nickelates, called layered square-planar nickelates, with the formula Nd$_{n+1}$Ni$_n$O$_{2n+2}$ (n = 5), also exhibits superconductivity with a similar T_c.[15] Furthermore, the pressurized ($\sim$ 15 GPa) Ruddlesden–Popper (RP) phase La$_3$Ni$_2$O$_7$ has been reported to exhibit superconductivity up to 80 K.[16] And superconductivity under pressure has also been observed in La$_4$Ni$_3$O$_{10}$.[17–21] The 80 K T_c observed in moderately pressurized RP nickelates leads to a new era for high-temperature superconductor families, often called as "nickel age" in a few perspective articles.[22–24] Figure 1 summarizes the trend of T_c progress over time for different nickelate subgroups.

Despite their electronic similarities to cuprates, nickelate superconductors exhibit distinct superconducting mechanisms. A primary distinction is the absence of bulk superconductivity in IL (IL) nickelates.[25] The topotactic reduction process is hard to produce thick superconducting films. And RP phases or other defects persist at the sample surface, hindering scanning probe techniques like scanning tunneling microscope/spectroscopy (STM/STS). This difficulty significantly impedes progress in understanding nickelate superconducting systems.

The combination of atomic spatial resolution and reasonable energy resolution makes aberration-corrected scanning transmission electron microscopy (AC-STEM) a powerful technique for investigating nickelate systems, as evidenced in many relevant strongly correlated oxide systems, including ferromagnetic,[26] ferroelectric[27,28] and superconducting systems.[29–31] There are a few reviews focusing on the physics and materials systems of superconducting nickelates,[32–35] but none focusing on the structure–property correlation in nickelates. In this review article, we will focus on STEM investigations on nickelate systems using various modes, such as high angle annual dark field (HAADF), annular bright-field (ABF), differential phase contrast (DPC), integrated DPC (iDPC), electron energy loss spectroscopy (EELS)

†Corresponding author. E-mail: licj@sustech.edu.cn

© 2024 Chinese Physical Society and IOP Publishing Ltd

and four dimensional-STEM ptychography (4D-STEM). We discuss (i) structural phase transition and spatial inhomogeneity during the topotactic reduction process, (ii) the electronic configuration and its connection to the polar $NdNiO_2/SrTiO_3$ interface, and (iii) structure–property relationships in extended nickelate systems, including layered square-planar and RP phase nickelate superconductors, as well as freestanding nickelate membranes. Finally, we want to make a perspective in terms of the future directions as from the phonon spectrum studies, which could reveal the true nature of the superconductivity in nickelate superconductors.

Structural aspects of superconducting IL nickelates

Figure 2(a) shows the initial structure of a pseudocubic 3D perovskite nickelate, $RNiO_3$ (R = Nd, Sr), represented by commonly corner-shared NiO_6 octahedra, which exhibit slight distortions. Upon the reduction by CaH_2 at 280 °C for four hours, the apical oxygen atoms are completely removed, as shown in Fig. 2(b). The in-plane lattice constant increases (from 3.81 Å to 3.92 Å), while the out-of-plane lattice constant decreases slightly (3.81 Å to 3.27 Å). This is consistent with a blue shift of the (002) peaks (Fig. 1(c)), which changes from pseudocubic to tetragonal symmetry.

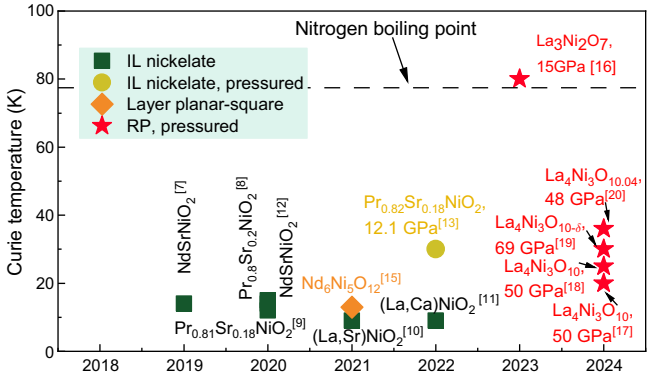


Fig. 1. The development of nickelate superconductors over the past 5 years. The T_c data is extracted from Refs. [7–20].

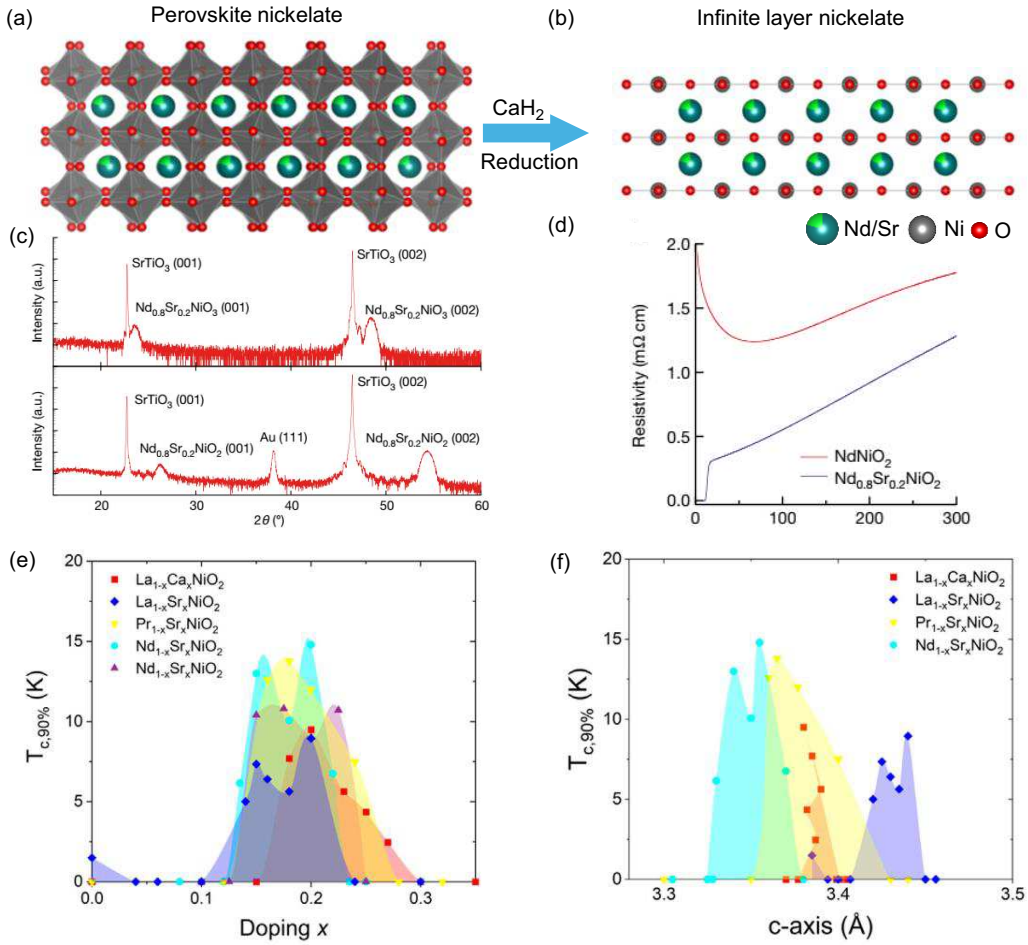


Fig. 2. Superconducting IL nickelates. (a) and (b) The crystal structures of $Nd_{1-x}Sr_xNiO_3$ and $Nd_{1-x}Sr_xNiO_2$, respectively. (c) The XRD spectra of $Nd_{1-x}Sr_xNiO_3$ and $Nd_{1-x}Sr_xNiO_2$ after CaH_2 reduction. (d) The resistance vs. temperature curve for $NdNiO_2$ and $Nd_{0.8}Sr_{0.2}NiO_2$ films, the latter shows superconducting transition at ∼ 14 K, adapted from Ref. [7]. (e)–(f) Superconducting phase diagrams of various hole doped IL nickelates, plotted as a function of hole doping levels x (e) and c-axis lattice constant (f), figure adapted from Ref. [36].

Without Sr substitution, $NdNiO_2$ exhibits semiconducting behavior with an obvious upturn when the temperature falls below 50 K. Upon Sr substitution (x = 0.2), it exhibits a superconducting transition at approximately 14 K (Fig. 1(d)), as first reported by Li *et al.*[7] Later, $Pr_{1-x}Sr_xNiO_2$[8] are successfully demonstrated to be super-

conducting. While (La,Sr)NiO_2 initially facing difficulties in achieving superconductivity,[7] it was eventually demonstrated by Zeng *et al.* in (La,Ca)NiO_2[11] and Osada *et al.* in (La, Sr)NiO_2 systems.[10] These findings indicate that rare-earth magnetism is not essential for superconductivity in IL nickelates. Both Zeng *et al.*[12] and Li *et al.*[13] reported similar phase diagram for $Nd_{1-x}Sr_xNiO_2$, revealing an optimum doping concentration of approximately $x = 0.2$. Notably, there is a dip in the critical temperature in La, Nd based IL superconductors, while this feature is absent in Pr-based superconducting series.[9] Chow *et al.*[36] summarized a correlation between T_c and *c*-lattice constant, suggesting that the lattice strain might be a key factor influencing superconductivity in these materials (Figs. 2(e) and 2(f)). The first observation of perfect diamagnetism was also reported by Zeng *et al.* in $Nd_{0.8}Sr_{0.2}NiO_2$ thin films, thus completing the other essential piece of evidence of Meissner effect, a hallmark of superconductivity.[37]

Topotactic reduction process STEM is a powerful tool for studying the reduction process and revealing the extent of apical oxygen removal. Puphal *et al.* reported the structure aspects of a single crystal $La_{1-x}Ca_xNiO_{2+\delta}$ sample[38] upon reduction. Figure 3(a) shows low-magnification HAADF-STEM images of the original perovskite network. The fast Fourier transformation (FFT) pattern indicates cubic symmetry, as expected. At higher magnification, figures 3(c) and 3(d) show the corresponding atomic scale HAADF and ABF images, revealing both apical and basal oxygen ions in the original ABF image. Upon reduction, the FFT pattern of the low-magnification HAADF image in Fig. 3(b) displays a rectangular feature. The atomic scale ABF image (Fig. 3(f)) clearly shows the absence of the apical oxygen atoms (noted the *c* axis pointing horizontally to the right) with some residual apical oxygen present locally. This is accompanied by the shrinkage of the *c*-lattice constant. The superimposed atomic models clearly illustrate the structural transition. Parzyck *et al.*[39] reported a multistage reduction process in nickelate films, observing a periodic removal of apical oxygen ions in intermediate reduced samples, resembling the $Nd_3Ni_3O_8$ structure. Han *et al.*[40] discovered a metal–insulator–superconductor transition by controlling the reduction duration. The intermediate insulating state is attributed to residual oxygen atoms in the Nd/Sr plane, disrupting the long-range order of the IL structure.

Unfortunately, perfect crystalline IL structure after the reduction process remains a challenge. In the early reports by Zeng *et al.*,[12] a good IL structure was maintained up to $\sim$ 10 nm from the (Nd,Sr)NiO_2/$SrTiO_3$ interface (Figs. 4(a) and 4(b)). However, in thicker films (35 nm), various defects, such as RP phases, emerge beyond the IL nickelate region (Figs. 4(c) and 4(d)). With advancements in thin film preparation technique and reduction process, the homogeneity of IL nickelate structure can be improved. *In-situ* Al reduction[41] or even direct hydrogen reduction using hydrogen ions[42] demonstrate atomic-scale uniformity at the surface, although the high quality reduced IL phase remains limited to the $\sim$ 10 nm scale. Due to the challenges associated with oxygen ion extraction, alternative approaches to stabilizing the IL phase directly (such as direct growth of $CoCuO_2$ phase[43]) should be explored.

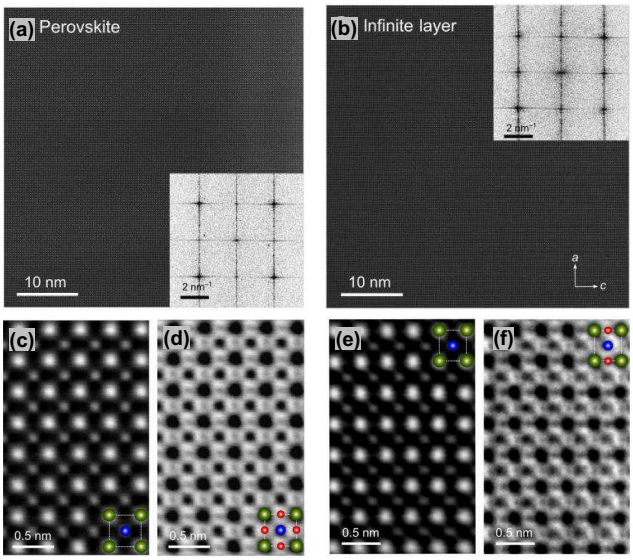


Fig. 3. Topotactic reduction of $La_{1-x}Ca_xNiO_3$ single crystals to $La_{1-x}Ca_xNiO_{2+\delta}$. Low-magnification HAADF images of the original perovskite structure (a) and reduced IL structure (b), insets are the fast Fourier transformation pattern (FFT). (c) and (d) Typical HAADF and ABF images of the zoomed region in (a), both apical and equatorial oxygens are present. (e) and (f) The HAADF and ABF images for the IL structure. Images adapted from Ref. [38].

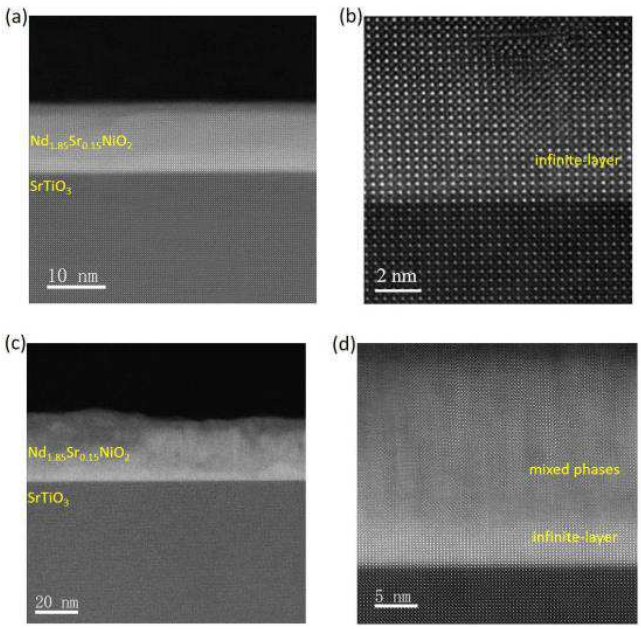


Fig. 4. The thickness of defect-free IL nickelate is limited to $\sim$ 10 nm. (a) and (b) HAADF images of 10 nm $Nd_{1.85}Sr_{0.15}NiO_2$ films, which are almost defect free. (c) and (d) HAADF images of 35 nm $Nd_{1.85}Sr_{0.15}NiO_2$ films. Only the interfacial region (less than 8 nm) exhibits good quality of the interlayer phase, while the upper layers show a mixed phase. Figure adapted from Ref. [12].

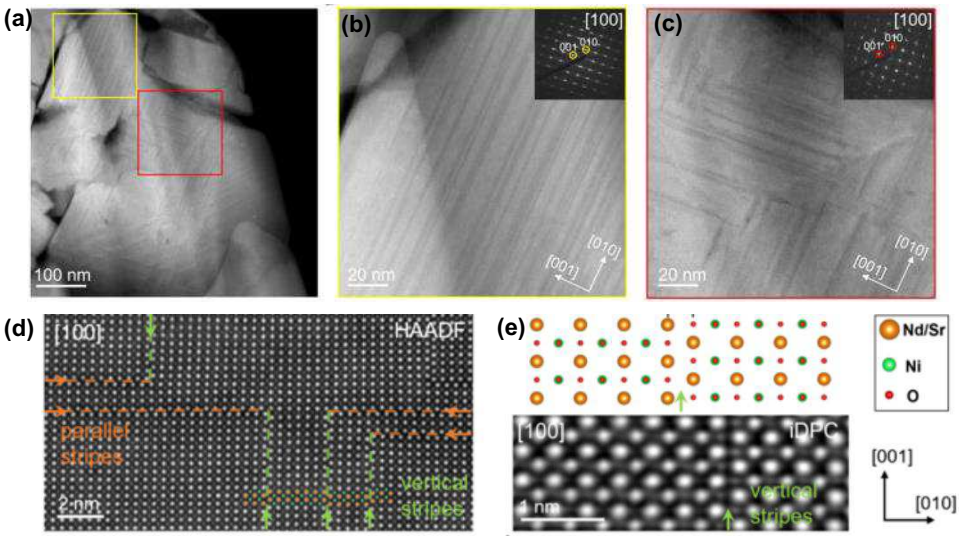


Fig. 5. STEM investigations of bulk IL $Nd_{0.8}Sr_{0.2}NiO_2$ polycrystals. (a)–(c) Low-magnification HAADF images of $Nd_{0.8}Sr_{0.2}NiO_2$ showing the parallel stripes (b) and perpendicular stripes (c). (d) Atomic resolution HAADF image of intersected stripes, breaking the IL structure. (e) The atomic structure and the iDPC image show the oxygen ion distribution across the vertical stripe, which shows a rock salt structure. Figure adapted from Ref. [44].

Absence of the bulk superconductivity Notably, bulk superconductivity in IL nickelates has yet to be observed.[25] Recent STEM-EELS studies have shed light on the atomic origins of this phenomenon.[44] Figure 5 displays parallel stripes along the [010] direction (Figs. 5(a) and 5(b)) in the bulk reduced sample ($Nd_{0.8}Sr_{0.2}NiO_2$), while other regions exhibit perpendicular stripes (Fig. 5(c)). The atomic-scale image (Fig. 5(d)) clearly resolves these intersecting stripes, which disrupt the IL structure. The atomic model is illustrated in Fig. 5(e). The acquired iDPC image reveals a rock salt structure within the vertical stripes. Polycrystalline $Nd_{0.8}Sr_{0.2}NiO_2$ is not only segmented by the grain boundaries but also disrupted by the stripe domains, hindering the observation of bulk superconductivity. Unexpected fluoride (F) impurities observed in reduced samples are found to be in the fluoride layer, but their roles need further investigation.

The absence of bulk superconductivity led to the suggestion that IL nickelate superconductivity might be an interfacial phenomenon, as proposed by a few theoretical studies.[45,46] Superconductivity has been observed on various substrates, including STO, LSAT[47] and NGO,[48] spanning both non-polar and polar interfaces, and even freestanding (La,Sr)NiO_2/STO[49] or (Nd,Sr)NiO_2/STO heterostructure membranes.[48] Hence, the lack of observed bulk superconductivity is likely due to limitations in material quality. A similar case exists in doped $LaNiO_2$ systems, where superconductivity was confirmed by Zeng *et al.*[11] after improving the quality of the parent perovskite thin films, initially thought to be non-superconducting. While exploring alternative approaches to stabilizing the IL structure beyond topotactic reactions is crucial, achieving higher quality bulk materials remains a priority.

EELS investigation The inhomogeneity of the IL structure, and the tendency for defect structures to segregate at the surface, STM studies on IL thin films remain challenging. EELS has also been frequently employed to investigate nickelates films and superlattices.[50] To reveal the electronic states of IL nickelates, Goodge *et al.* conducted systematic EELS spectrum imaging on IL nickelate thin films.[51–54] A uniform distribution of Nd and Ni elements is observed by EELS mapping, and an atomically abrupt $NdNiO_2/SrTiO_3$ interface is evident in Figs. 6(a) and 6(b). As shown in Fig. 6(c), the oxygen *K* edge is sensitive to the reduction process, with the reference spectra of the NiO (Ni^{2+}), bulk $NdNiO_3$ (Ni^{3+}) and $SrTiO_3$ (Ti^{4+}) (marked as black spectra). The acquired O *K*-edge spectrum for $NdNiO_3$ shows a characteristic pre-peak at $\sim$ 527 eV, and it is suppressed upon gradual reduction ($NdNiO_{2+\delta}$). The pre-peak disappears in $NdNiO_2$ (Fig. 6(d)), consistent with previous x-ray absorption spectroscopy studies.[55] Both EELS and XAS results suggest that the oxygen 2p band is located below the lower Hubbard band (LHB). This contrasts with cuprates, where oxygen 2p band lies between the LHB and upper Hubbard band (UHB), as shown in Fig. 6(e). It is worthy nothing that, in regions where $NdNiO_2$ and $NdNiO_3$ coexist, the pre-peak reappears, creating ambiguity in extracting electronic state information in reduced samples.

Upon Sr doping in $NdNiO_2$, the Sr^{2+} ions introduce holes into the system, evidenced by the emergence of a shallow pre-peak at 528 eV, corresponding to hole doping. This pre-peak gradually intensifies with increasing Sr content (Fig. 6(f)). Compared to YBCO, the hole doping peak at 527 eV is less pronounced,[56] supporting the picture of larger charge transfer gaps in nickelates,[57] as illustrated in Fig. 6(e). The weak pre-peak arises from weak Ni 3d and O 2p hybridization, as suggested by Karp *et al.*[58] The Ni $L_{2,3}$ peak exhibits a slight

rightward shift in the doped samples (Fig. 6(g)), similar to the Nd $N_{2,3}$ peaks (Fig. 6(h)). This deviates from the typical trend in transition metal oxides, where the EELS spectra generally shift to lower energies upon reduction of the cation valence.[59] The correlated changes in the O, Ni and Nd spectra indicate a multi-band electronic structure with Mott–Hubbard characteristics in IL nickelates. Hole doping influences not only the oxygen p-bands but also the Ni and Nd d-bands.

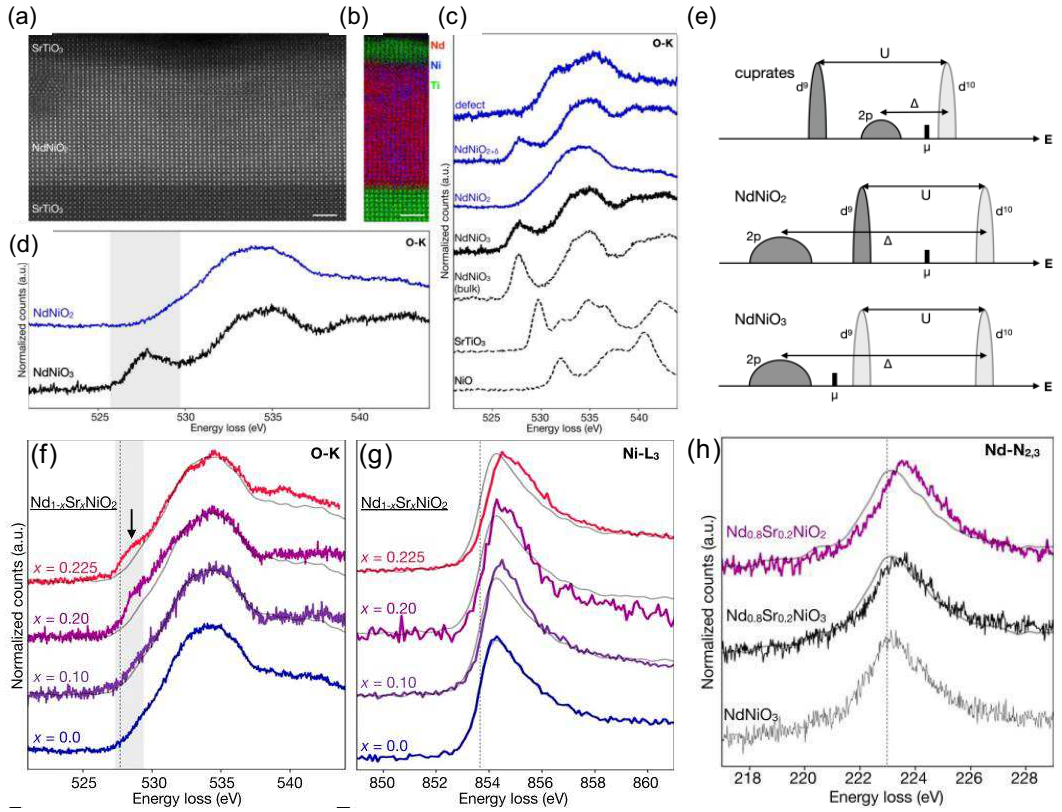


Fig. 6. EELS of doped $NdNiO_2$ thin films. (a) and (b) HAADF and EELS mapping results of the STO/$NdNiO_2$/STO heterostructures. (c) and (d) The characteristic oxygen K edge before and after the reduction, with STO, NiO reference spectra added as control spectra. (e) Schematic Zaanen–Sawatzky–Allen electronic structure comparison between the cuprates, IL nickelate and $NdNiO_3$. (f)–(h) O K edge, Ni $L_{2,3}$ and Nd $N_{2,3}$ edges of $Nd_{1-x}Sr_xNiO_2$ with x ranging from 0 to 0.225, respectively. Figures adapted from Ref. [51].

Polar interface Atomic-resolution EELS effectively reveals the polar nature of the interface between IL nickelate films and STO interface. $NdNiO_2$ consists of alternating charged layers of $[Nd]^{3+}$ and $[NiO_2]^{3-}$, forming a polar/nonpolar interface with STO. With increasing film thickness, electronic and atomic reconstructions are expected to occur.[60] Experimentally, Goodge *et al.*[61] conducted a careful analysis of $Nd_{1-x}Sr_xNiO_2$/STO interface, finding that a single intermediate Nd(Ti,Ni)O_3 layer forms at the interface, mitigating the energy instability arising from the polar discontinuity. Chao *et al.* reported EELS spectrum imaging on STO/$NdNiO_{2+\delta}$ superlattices with varying periodicity,[62] revealing nonuniform distribution of residual apical oxygen atoms in the IL $NdNiO_{2+\delta}$. Consistently, atomic-scale EELS studies show that Ni valence is between Ni^{1+} and Ni^{2+}, while Ti remains majorly Ti^{4+} aligning with Goodge's observations.[51] An additional observation is the enhanced displacement of Ni atoms near the STO/$NdNiO_{2+\delta}$ interface when $NdNiO_{2+\delta}$ is beyond 4 uc. This displacement is thought to minimize the polar discontinuity.

In addition to the polar interface, surface reconstruction due to IL nickelate has been observed in $Pr_{0.8}Sr_{0.2}NiO_{2+\delta}$ thin films grown on polar $NdGaO_3$ substrates,[63] though this system is not superconducting. Using EELS mapping and 4D-STEM, Yang *et al.* directly imaged the local atomic electric field surrounding Ni atoms near the surface, revealing significant surface reconstruction in the partially reduced nickelate thin films.[63] The HAADF image of $Pr_{0.8}Sr_{0.2}NiO_{2+\delta}$ is given in Fig. 7(a). Figure 7(b) shows the uc-by-uc oxygen K edge peak evolution from the interface to surface, as summarized in Fig. 7(c). The top 4 unit cells show a reduced A/B peak intensity ratio, which is consistent with the increasing L_3/L_2 ratio of the Ni $L_{2,3}$ edge (Fig. 7(e)). Both oxygen K edge and Ni L edge confirm the reduction of the Ni valence from Ni^{3+} to Ni^{2+} in the outmost 4 unit cells, as summarized in Figs. 7(c) and 7(d).

The reconstructed atomic-column-resolved ADF image and electric field images (Figs. 8(a) and 8(b), respectively) reveal an increase of the electric field strength near the Ni atoms (Figs. 8(c) and 8(d)), consistent with Ni valence change trend

near the sample surface. The enhanced Ni–O displacement (calculated from basal NiO_2 atomic plane in ABF images) at the outmost four unit cells of $Pr_{0.8}Sr_{0.2}NiO_{2+\delta}$ films confirms the surface polar constructions. Combination of STEM-ABF, 4D-STEM, and EELS enables simultaneous probing of local structural and charge distribution information, providing guidance for understanding polarity at the atomic scale in nickelates.

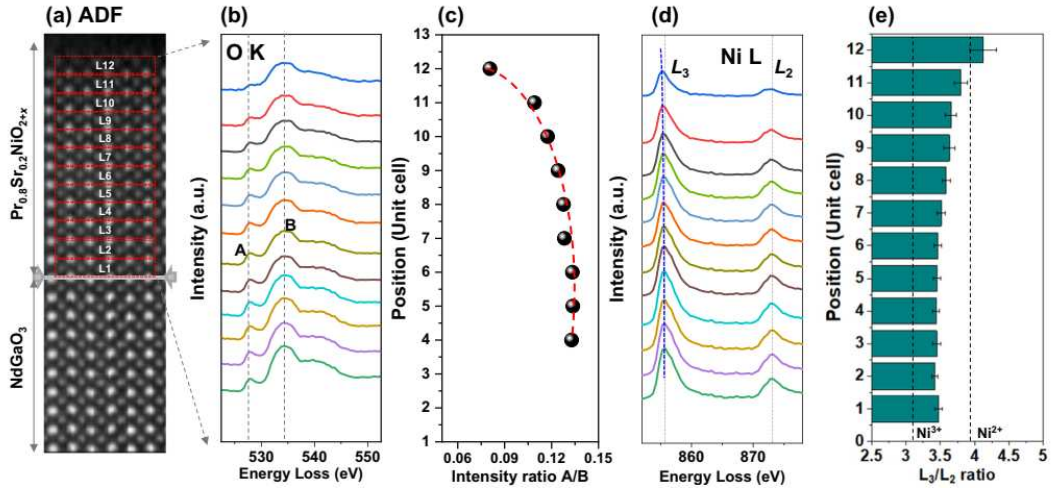


Fig. 7. EELS characterization of the surface reconstruction in $Pr_{0.8}Sr_{0.2}NiO_{2+\delta}/NdGaO_3$ heterostructures. (a) Atomic scale HAADF image, (b) O *K* edge spectra across the $Pr_{0.8}Sr_{0.2}NiO_{2+\delta}/NdGaO_3$ interface. (c) The uc-by-uc peak A and B intensity ratio extracted from panel (b). (d) The uc-by-uc Ni $L_{2,3}$ edge acquired from region in panel (a), and (e) the extracted L_3/L_2 intensity ratio from panel (d). Adapted from Ref. [63].

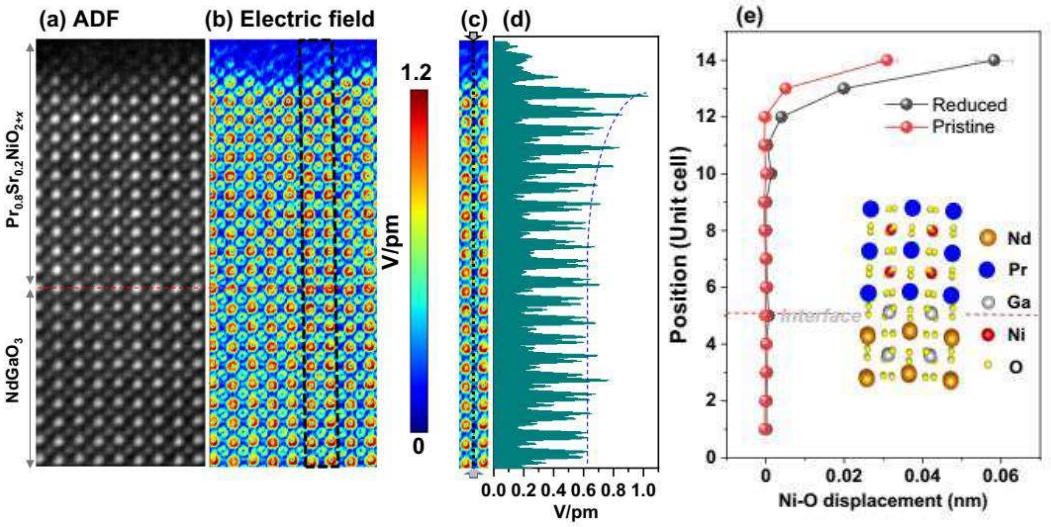


Fig. 8. The 4D-STEM image across the $Pr_{0.8}Sr_{0.2}NiO_{2+\delta}/NdGaO_3$ interface to reveal the surface reconstruction. (a) and (b) Reconstructed ADF and reconstructed electric field map from 4D-STEM technique. (c) The electric field map extracted from dashed rectangle enclosed in panel (b). (d) The line profile of the electric field distribution of the B-site atom positions from panel (c). (e) The measured Ni–O placement showing an increase at the surface 4 ucs. Figures adapted from Ref. [63].

Layered square-planar nickelate superconductivity Undoped $NdNiO_2$ belongs to a series of layered square-planar nickelates with chemical formula $Nd_{n+1}Ni_nO_{2n+2}$ and is known as the 'IL' ($n = \infty$) nickelate. It is obtained by reducing the corresponding RP phase, which has the general form of $Nd_{n+1}Ni_nO_{3n+1}$.[64] Pan *et al.*[15] reported the first observation of superconducting quintuple-layer square-planar nickelate with $T_c \sim 13$ K in $Nd_6Ni_5O_{12}$. This compound has an effective Ni $d^{8.8}$ band filling, which coincides with optimal doping range of the nickelate system (Fig. 9(a)). In comparison, $Nd_4Ni_3O_8$ does not show any sign of superconductivity because its electronic filling ($d^{8.67}$) lies in the overdoped regime (Fig. 9(b)). HAADF and ABF STEM images (Fig. 9(c)) confirm the high quality of quintuple-layer square lattice. Upon removal of apical oxygen atoms, the conductivity of this layered square-planar nickelate could be tuned by the epitaxial strain.[65] The advantage of the multiple layered square-planar nickelate system is that it does not require additional chemical doping to achieve superconductivity, providing a new route for expanding the nickelate superconductors.

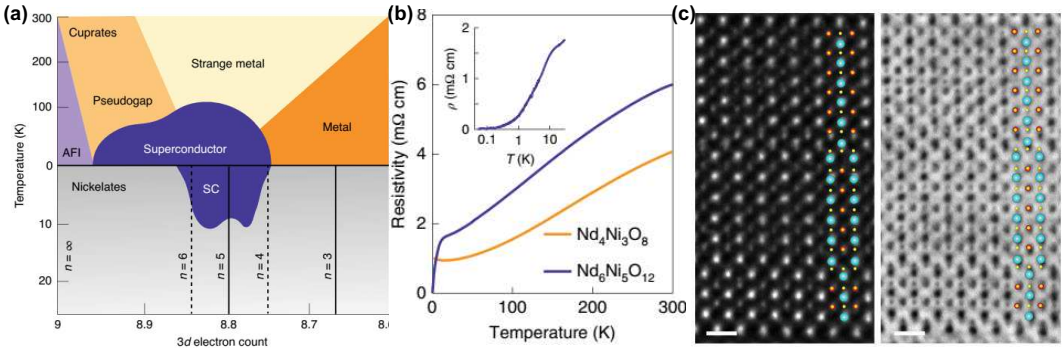


Fig. 9. Superconducting layered square-planar nickelates. (a) A comparison of the IL nickelate superconductor phase diagram between the cuprates and nickelates, with the addition correspondence between n in $Nd_{n+1}Ni_nO_{2n+2}$ and the Ni 3d electronic filing status. (b) The resistivity versus temperature curve for $Nd_4Ni_3O_8$ and $Nd_6Ni_5O_{12}$, respectively, inset figure shows the curve of $Nd_6Ni_5O_{12}$ with temperature plotted in log scale. (c) The HAADF and ABF images of the $Nd_6Ni_5O_{12}$. Figure adapted from Ref. [15].

Freestanding superconducting IL nickelates While bulk superconductivity in IL nickelates has not yet been achieved, both Lee *et al.*[48] and Yan *et al.*[49] successfully reported that superconductivity is retained in freestanding (Nd,Sr)NiO_2/STO heterostructures ($T_c \sim 10.9$ K). The STO/(Nd,Sr)NiO_2/STO heterostructure cross-sectional and plane-view HAADF images show that the high quality thin film is maintained after the transfer process (Figs. 10(a) and 10(b)). Geometrical phase analysis of the strain shows that certain RP phase remains (marked as square patterns). A slight decrease in T_c is observed in released thin films, regardless of whether they are released from STO or $NdGaO_3$ substrates, as shown in Figs. 10(c) and 10(d). The realization of the freestanding nickelate superconductors provides an ideal platform for studying the effect of strain and conducting atomic-scale investigations by eliminating the substrate effect.

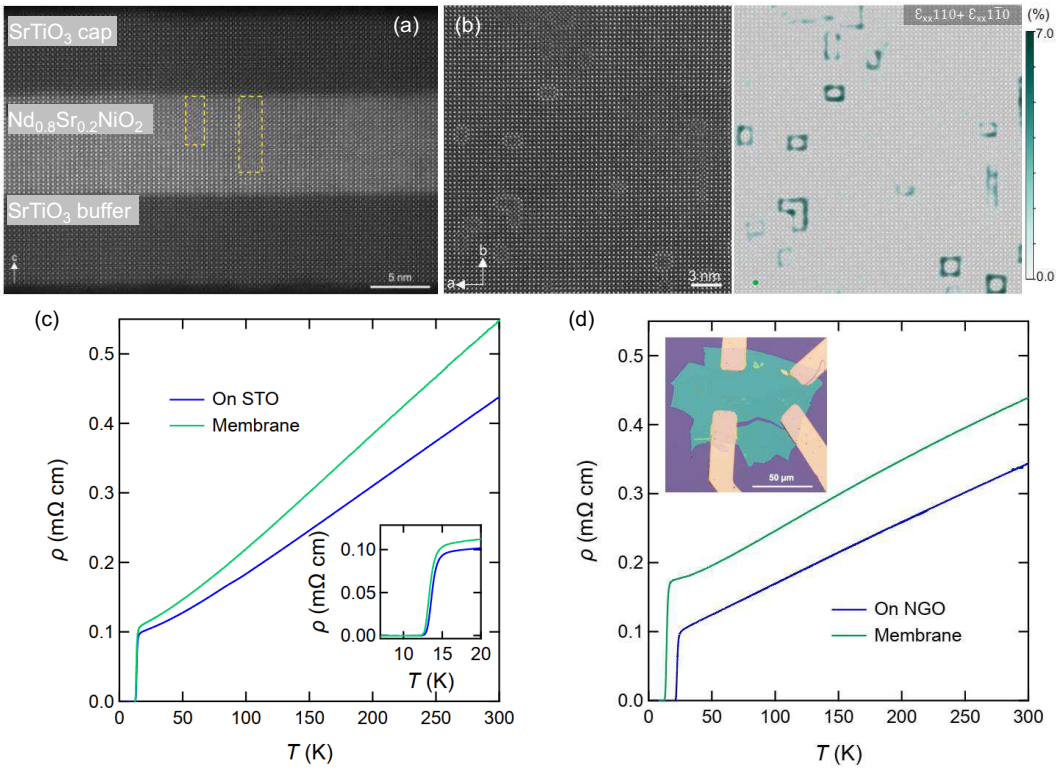


Fig. 10. Superconducting IL nickelate freestanding membranes. HAADF images of (a) the cross-section of freestanding STO/$Nd_{0.8}Sr_{0.2}NiO_2$/STO membrane. (b) The plane-view of the same sample and corresponding strain mapping revealing the RP faults, (c) the resistivity versus temperature curves of the freestanding membrane compared to that on STO substrates and (d) on NGO substrates. Inset of (d) shows the released freestanding superconducting IL nickelate membranes. Figures adapted from Ref. [48].

Ruddlesden–Popper nickelate superconductivity A nickelate superconductor with a high T_c of ~ 80 K was recently reported in single crystals of the RP phase ($n = 2$), $La_3Ni_2O_7$, under pressures between 14.0 GPa and 43.5 GPa.[16] This finding was quickly replicated in polycrystalline systems.[66] The T_c is significantly higher than the iron-based superconductors and IL nickelates. Later, $La_4Ni_3O_{10}$ was also reported to be superconducting under pressure.[17–21]

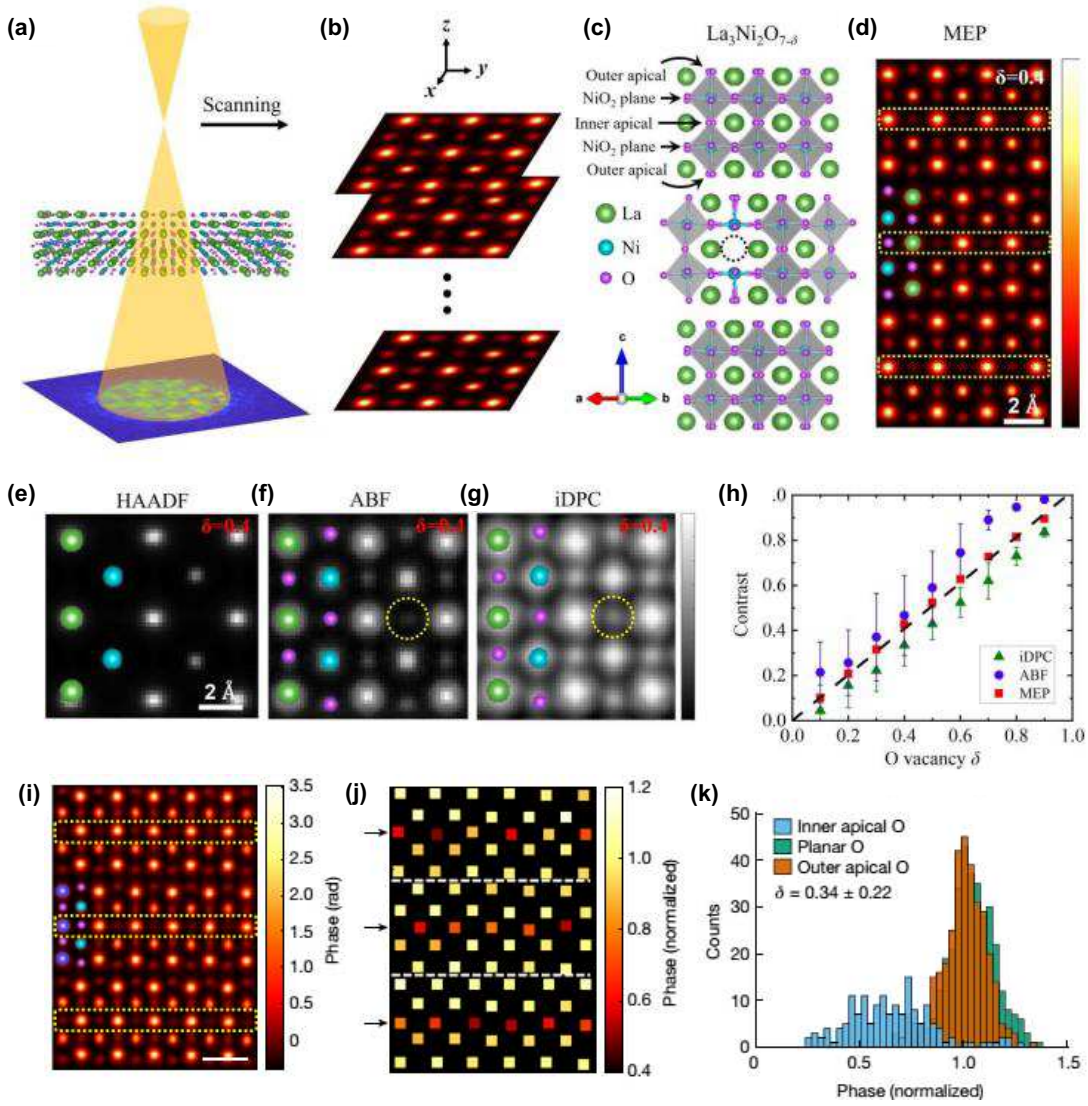


Fig. 11. Visualization of apical oxygen vacancies in $La_3Ni_2O_{7-\delta}$ using MEP technique. (a) A schematic setup of MEP technique, (b) illustration of the reconstructed three-dimensional object with MEP. Specifically, the z axis refers to the depth dimension. (c) A structural model of $La_3Ni_2O_{7-\delta}$, (d) a simulated projected MEP image for $\delta = 0.4$, (e)–(g) simulated HAADF (e), ABF (f) and iDPC (g) images for $\delta = 0.4$ with atomic models imposed on top. (h) The oxygen vacancy concentration effect on the simulated image contrast of oxygen atom columns in MEP, iDPC, and ABF modes, respectively. (i) Projected MEP phase image and (j) color-coded maps for the phases of O columns. (k) A histogram of phases from different oxygen sites. Figure adapted from Ref. [67].

The origin of superconductivity is drastically different in at least two aspects: (i) in a perfect IL nickelate, Ni is in Ni^{+} ($3d^9$) state, while in PR nickelate, for example, $La_3Ni_2O_7$, Ni is in $Ni^{2.5+}$ ($3d^{7.5}$) state. (ii) Apical oxygen atoms are missing in IL nickelate, while they are present in RP nickelate. In the IL nickelate, the inter layer coupling is weak. In contrast, strong inter-layer coupling of $3d_{z^2}$ orbital and apical oxygen anions is critical to promote superconductivity under pressure.

To investigate the structural and electronic properties of this newly discovered superconducting system, Dong *et al.*[67] developed an energy-filtered multi-slice electron ptychography (MEP) technique (Figs. 11(a) and 11(b)), where the reconstructed phase is found to be sensitive to oxygen vacancies (Figs. 11(c) and 11(d)), revealing that oxygen vacancies are primarily occupied in the inner apical sites (as seen in Figs. 11(i) and 11(j)). By scanning a defocused electron probe across the sample, 4D-STEM datasets are recorded, and the MEP image is reconstructed with superior resolution compared to ABF and iDPC images (Figs. 11(e) and 11(f)). MEP also exhibits a better linear relationship for quantitative analysis compared to iDPC and ABF techniques (Fig. 11(h)). These results are consistent with atomic-scale EELS observations across the three NiO layers and suggest that $La_3Ni_2O_7$ superconductivity falls within a charge transfer picture, unlike the Mott–Hubbard picture in IL nickelate superconductors.

2. Discussion and perspective

Nickelate superconductors, including IL layered structures and RP phases, have opened a new playground for exploring high temperature superconductors. Conventional STEM, with HAADF and ABF imaging modes, has been ex-

tremely valuable in identifying the spatial distribution of responsible phases and any associated defects. A few key implications worth mentioning are given below.

(i) The microstructures revealed via STEM are insightful to improving the sample quality. For example, in the IL nickelates, STEM imaging has played vital roles in establishing the correspondence between the growth condition, substrate choice, the reduction conditions and the superconducting property. The oxygen vacancies distributions from STEM observations in $La_3Ni_2O_7$ would provide guidance to the sample growth and better reduction processes.

(ii) Superconductivity is primarily governed by electronic properties, the atomic-scale spatial resolution EELS mapping has provided significant insights into the Ni electronic valence and the degree of hybridization between the Nd 3d and oxygen 2p orbitals. The evolution of hole doping into the oxygen *K*-edge clearly reveals the difference between nickelates and cuprates in terms of the charge transfer model.

Nevertheless, several challenges remain.

(I) Due to the topotactic reduction process is still not well controlled, the remaining apical oxygen results in partially reduced nickelates, which leads to complications in the hole doping in the IL nickelates. The quantification of the apical oxygen content is still challenging using ABF, iDPC or EELS mapping. The newly developed MEP based on 4D-STEM technique shows promising routes to quantification of the local stoichiometry, as proved to be useful to quantify the position-dependent apical oxygen vacancies in oxygen deficient RP phase. However, it shows rather large uncertainty due to inhomogeneous distribution of the oxygen vacancies, further standard samples with uniformly distributed oxygen stoichiometry should be found to validate the accuracy of the measured values, and the oxygen vacancy detection limits to be evaluated.

(II) The correlation between the oxygen content, Ni valence, lattice constant and atomic distortion should be more closely monitored in nickelate systems. With the emergence of 4D-STEM, the reconstructed atomic scale electric field provides a unique perspective to study the charge distribution within nickelate systems. The consistency between different techniques should always be considered to exclude extrinsic artifacts.

(III) The emerging 4D-EELS technique[68] provides a promising approach to examine the phonon dispersion of the IL nickelate superconductors at nanometer scale, which could effectively account for the structural inhomogeneity in thin film nickelates. The nanometer resolved phonon dispersion spectra could be extremely important to uncover and verify the proposed unconventional pairing mechanisms[69–71] in nickelate superconductors.

(IV) For strongly correlated systems, a strong microstructure–property correlation is still lacking. Correlated characterization techniques across different length scales are necessary. For example, combining Kelvin probe force microscopy (KPFM), scanning tunning microscopy (STM) and STEM together would reveal insights from the surface potential, density of states and electronic structure perspective.

To conclude, STEM techniques provide unique atomic and electronic structure insights into nickelate superconductors, particularly given the inherent inhomogeneity in topotactically reduced nickelates. The similarity and difference between IL, layered planar-square and RP phase nickelates superconductivity require additional systematic investigations from the microscopic perspective. The emerging ptychographic 4D-STEM technique has been proving to be extremely important to map atomic scale electric field and nanoscale oxygen off-stoichiometry. We believe 4D EELS would contribute significantly to understanding the pairing mechanisms in these fascinating nickelate superconducting systems.

Acknowledgments

C. Li acknowledges the insightful discussions with Prof. Dongsheng Song. Project supported by the National Natural Science Foundation of China (Grant No. 52172115), the Guangdong Provincial Key Laboratory Program from the Department of Science and Technology of Guangdong Province (Grant No. 2021B1212040001), Guangdong Basic and Applied Basic Research Foundation (Grant No. 2022A1515012434), Shenzhen Science and Technology Program (Grant No. 20231121093057002), and Natural Science Foundation of Guangdong Province, China (Grant No. 2022A1515010762).

References

[1] Chaloupka J and Khaliullin G 2008 *Phys. Rev. Lett.* **100** 016404
[2] Crespin M, Levitz P and Gatineau L 1983 *J. Chem. Soc.-Faraday Trans.* **79** 1181
[3] Levitz P, Crespin M and Gatineau L 1983 *J. Chem. Soc.-Faraday Trans.* **79** 1195
[4] Hayward M A and Rosseinsky M J 2003 *Solid State Sci.* **5** 839
[5] Kawai M, Inoue S, Mizumaki M, Kawamura N, Ichikawa N and Shimakawa Y 2009 *Appl. Phys. Lett.* **94** 082102
[6] Ikeda A, Krockenberger Y, Irie H, Naito M and Yamamoto H 2016 *Appl. Phys. Express* **9** 061101
[7] Li D, Lee K, Wang B Y, Osada M, Crossley S, Lee H R, Cui Y, Hikita Y and Hwang H Y 2019 *Nature* **572** 624
[8] Osada M, Wang B Y, Goodge B H, Lee K, Yoon H, Sakuma K, Li D, Miura M, Kourkoutis L F and Hwang H Y 2020 *Nano Lett.* **20** 5735
[9] Osada M, Wang B Y, Lee K, Li D and Hwang H Y 2020 *Phys. Rev. Mater.* **4** 121801
[10] Osada M, Wang B Y, Goodge B H, Harvey S P, Lee K, Li D, Kourkoutis L F and Hwang H Y 2021 *Adv. Mater.* **33** 2104083
[11] Zeng S, Li C, Chow L E, Cao Y, Zhang Z, Tang C S, Yin X, Lim Z S, Hu J, Yang P and Ariando A 2022 *Sci. Adv.* **8** eabl9927
[12] Zeng S, Tang C S, Yin X, Li C, Li M, Huang Z, Hu J, Liu W, Omar G J, Jani H, Lim Z S, Han K, Wan D, Yang P, Pennycook S J, Wee A T S and Ariando A 2020 *Phys. Rev. Lett.* **125** 147003

[13] Li D, Wang B Y, Lee K, Harvey S P, Osada M, Goodge B H, Kourkoutis L F and Hwang H Y 2020 *Phys. Rev. Lett.* **125** 027001
[14] Wang N N, Yang M W, Yang Z, Chen K Y, Zhang H, Zhang Q H, Zhu Z H, Uwatoko Y, Gu L, Dong X L, Sun J P, Jin K J and Cheng J G 2022 *Nat. Commun.* **13** 4367
[15] Pan G A, *et al.* 2022 *Nat. Mater.* **21** 160
[16] Sun H, Huo M, Hu X, Li J, Liu Z, Han Y, Tang L, Mao Z, Yang P, Wang B, Cheng J, Yao D X, Zhang G M and Wang M 2023 *Nature* **621** 493
[17] Li Q, Zhang Y J, Xiang Z N, Zhang Y, Zhu X and Wen H H 2024 *Chin. Phys. Lett.* **41** 017401
[18] Zhang M, *et al.* 2023 arXiv: 2311.07423 [cond-mat]
[19] Zhu Y, *et al.* 2024 *Nature* **631** 531
[20] Nagata H, Sakurai H, Ueki Y, Yamane K, Matsumoto R, Terashima K, Hirose K, Ohta H, Kato M and Takano Y 2024 arXiv: 2405.19880 [cond-mat]
[21] Sakakibara H, Ochi M, Nagata H, Ueki Y, Sakurai H, Matsumoto R, Terashima K, Hirose K, Ohta H, Kato M, Takano Y and Kuroki K 2024 *Phys. Rev. B* **109** 144511
[22] Botana A S, Lee K W, Norman M R, Pardo V and Pickett W E 2022 *Front. Phys.* **9** 813532
[23] Pickett W E 2021 *Nat. Rev. Phys.* **3** 7
[24] Norman M R 2020 *Physics* **13** 85
[25] Li Q, He C, Si J, Zhu X, Zhang Y and Wen H H 2020 *Commun. Mater.* **1** 16
[26] Li M, Tang C, Paudel T R, Song D, Lü W, Han K, Huang Z, Zeng S, Renshaw Wang X, Yang P, Ariando, Chen J, Venkatesan T, Tsymbal E Y, Li C and Pennycook S J 2019 *Adv. Mater.* **31** 1901386
[27] Li M, Chen P, Zhang Y, Zhang Y, Liu Z, Tang C, Chung J Y, Gu M, Li J, Huang Z, Chow G M, Li C and Pennycook S J 2023 *Small* **19** 2203201
[28] Li M, Huang Z, Tang C, Song D, Mishra T P, Ariando A, Venkatesan T, Li C and Pennycook S J 2019 *Adv. Funct. Mater.* **29** 1906655
[29] Pennycook S J, Li C, Li M, Tang C, Okunishi E, Varela M, Kim Y M and Jang J H 2018 *J. Anal. Sci. Technol.* **9** 11
[30] Wu H, Zhao X, Guan C, Zhao L D, Wu J, Song D, Li C, Wang J, Loh K P, Venkatesan T V and Pennycook S J 2018 *Adv. Mater.* **30** 1802402
[31] Gázquez J, Sánchez-Santolino G, Biškup N, Roldán M A, Cabero M, Pennycook S J and Varela M 2017 *Mater. Sci. Semicond. Process.* **65** 49
[32] Zhou X, Qin P, Feng Z, Yan H, Wang X, Chen H, Meng Z and Liu Z 2022 *Mater. Today* **55** 170
[33] Wang B Y, Lee K and Goodge B H 2024 *Annu. Rev. Condens. Matter Phys.* **15** 305
[34] Yang X, Li M, Ding Z, Li L, Ji C and Wu G 2023 *Adv. Quantum Technol.* **6** 2200065
[35] Nomura Y and Arita R 2022 *Rep. Prog. Phys.* **85** 052501
[36] Chow L E and Ariando A 2022 *Front. Phys.* **10** 834658
[37] Zeng S W, Yin X M, Li C J, Chow L E, Tang C S, Han K, Huang Z, Cao Y, Wan D Y, Zhang Z T, Lim Z S, Diao C Z, Yang P, Wee A T S, Pennycook S J and Ariando A 2022 *Nat. Commun.* **13** 743
[38] Puphal P, Wu Y M, Fürsich K, Lee H, Pakdaman M, Bruin J a N, Nuss J, Suyolcu Y E, Van Aken P A, Keimer B, Isobe M and Hepting M 2021 *Sci. Adv.* **7** eabl8091
[39] Parzyck C T, Gupta N K, Wu Y, Anil V, Bhatt L, Bouliane M, Gong R, Gregory B Z, Luo A, Sutarto R, He F, Chuang Y D, Zhou T, Herranz G, Kourkoutis L F, Singer A, Schlom D G, Hawthorn D G and Shen K M 2024 *Nat. Mater.* **23** 486
[40] Han K, Xie M, Mei Y, Lin R, Xu L, Chen P, Yin P, Zeng S, Ge B and Ariando A 2023 *Appl. Phys. Lett.* **123** 182601
[41] Wei W, Shin K, Hong H, Shin Y, Thind A S, Yang Y, Klie R F, Walker F J and Ahn C H 2023 *Phys. Rev. Mater.* **7** 013802
[42] Sun W, Wang Z, Hao B, Yan S, Sun H, Gu Z, Deng Y and Nie Y 2024 *Adv. Mater.* **36** 2401342
[43] Azuma M, Hiroi Z, Takano M, Bando Y and Takeda Y 1992 *Nature* **356** 775
[44] Hu K, Li Q, Song D, Jia Y, Liang Z, Wang S, Du H, Wen H H and Ge B 2024 *Nat. Commun.* **15** 5104
[45] Bernardini F and Cano A 2020 *J. Phys.: Mater.* **3** 03LT01
[46] He R, Jiang P, Lu Y, Song Y, Chen M, Jin M, Shui L and Zhong Z 2020 *Phys. Rev. B* **102** 035118
[47] Ren X, Li J, Chen W C, Gao Q, Sanchez J J, Hales J, Luo H, Rodolakis F, Mcchesney J L, Xiang T, Hu J, Comin R, Wang Y, Zhou X and Zhu Z 2023 *Commun. Phys.* **6** 341
[48] Lee Y, Wei X, Yu Y, Bhatt L, Lee K, Goodge B H, Harvey S P, Wang B Y, Muller D A, Kourkoutis L F, Lee W S, Raghu S and Hwang H Y 2024 arXiv: 2402.05104 [cond-mat]
[49] Yan S, Mao W, Sun W, Li Y, Sun H, Yang J, Hao B, Guo W, Nian L and Gu Z 2024 arXiv: 2401.15980 [cond-mat]
[50] Gauquelin N, Benckiser E, Kinyanjui M K, Wu M, Lu Y, Christiani G, Logvenov G, Habermeier H U, Kaiser U, Keimer B and Botton G A 2014 *Phys. Rev. B* **90** 195140
[51] Goodge B H, Li D, Lee K, Osada M, Wang B Y, Sawatzky G A, Hwang H Y and Kourkoutis L F 2021 *Proc. Natl. Acad. Sci. USA* **118** e2007683118
[52] Gibert M, Viret M, Torres-Pardo A, Piamonteze C, Zubko P, Jaouen N, Tonnerre J M, Mougin A, Fowlie J, Catalano S, Gloter A, Stéphan O and Triscone J M 2015 *Nano Lett.* **15** 7355
[53] Gauquelin N, Benckiser E, Kinyanjui M K, Wu M, Lu Y, Christiani G, Logvenov G, Habermeier H U, Kaiser U, Keimer B and Botton G A 2014 *Phys. Rev. B* **90** 195140
[54] Wang L, Zhang Q, Chang L, You L, He X, Jin K, Gu L, Guo H, Ge C, Feng Y and Wang J 2017 *Adv. Electron. Mater.* **3** 1700321
[55] Hepting M, *et al.* 2020 *Nat. Mater.* **19** 381
[56] Gauquelin N, Hawthorn D G, Sawatzky G A, Liang R X, Bonn D A, Hardy W N and Botton G A 2014 *Nat. Commun.* **5** 4275
[57] Jiang M, Berciu M and Sawatzky G A 2020 *Phys. Rev. Lett.* **124** 207004
[58] Karp J, Botana A S, Norman M R, Park H, Zingl M and Millis A 2020 *Phys. Rev. X* **10** 021061
[59] Tan H, Verbeeck J, Abakumov A and Van Tendeloo G 2012 *Ultramicroscopy* **116** 24
[60] He R, Jiang P, Lu Y, Song Y, Chen M, Jin M, Shui L and Zhong Z 2020 *Phys. Rev. B* **102** 035118
[61] Goodge B H, Geisler B, Lee K, Osada M, Wang B Y, Li D, Hwang H Y, Pentcheva R and Kourkoutis L F 2023 *Nat. Mater.* **22** 466
[62] Yang C, Ortiz R A, Wang Y, Sigle W, Wang H, Benckiser E, Keimer B and Van Aken P A 2023 *Nano Lett.* **23** 3291
[63] Yang C, Pons R, Sigle W, Wang H, Benckiser E, Logvenov G, Keimer B and Van Aken P A 2024 *Nat. Commun.* **15** 378
[64] Zhang J and Tao X 2021 *CrystEngComm* **23** 3249
[65] Ferenc Segedin D, Goodge B H, Pan G A, Song Q, Labollita H, Jung M C, El-Sherif H, Doyle S, Turkiewicz A, Taylor N K, Mason J A, N'diaye A T, Paik H, El Baggari I, Botana A S, Kourkoutis L F, Brooks C M and Mundy J A 2023 *Nat. Commun.* **14** 1468
[66] Wang G, Wang N N, Shen X L, Hou J, Ma L, Shi L F, Ren Z A, Gu Y D, Ma H M, Yang P T, Liu Z Y, Guo H Z, Sun J P, Zhang G M, Calder S, Yan J Q, Wang B S, Uwatoko Y and Cheng J G 2024 *Phys. Rev. X* **14** 011040
[67] Dong Z, Huo M, Li J, Li J, Li P, Sun H, Gu L, Lu Y, Wang M, Wang Y and Chen Z 2024 *Nature* **630** 847
[68] Wu M, Shi R, Qi R, Li Y, Du J and Gao P 2023 *Ultramicroscopy* **253** 113818
[69] Meier Q N, De Vaulx J B, Bernardini F, Botana A S, Blase X, Olevano V and Cano A 2024 *Phys. Rev. B* **109** 184505
[70] Di Cataldo S, Worm P, Si L and Held K 2023 *Phys. Rev. B* **108** 174512
[71] Ding X, *et al.* 2023 *Nature* **615** 50